1

2   Pavement cell shape quantification with LobeFinder

3

4

5   Corresponding authors:

6   David Umulis, 225 S. University St., Purdue University, West Lafayette, IN 47907 USA, (765)

7   494-1223, dumulis@purdue.edu

8

9   Dan Szymanski, 915 W. State Street, Purdue University, West Lafayette, IN 47907 USA, (765)

10   494-8092, dszyman@purdue.edu

11   Research Area: Breakthrough Technologies

12

13

14

15

LobeFinder: a convex hull-based method for quantitative boundary analyses of lobed plant cells

18

19

20

21

22

23

Tzu-Ching Wu[1,*], Samuel A. Belteton[2,*], Jessica Pack[1], Daniel B Szymanski[2, 3, 4], David M. Umulis[1,5]

[1]Department of Agricultural and Biological Engineering, 225 S. University St., Purdue University, West Lafayette, IN 47907 USA

[2]Department of Botany and Plant Pathology, 915 W. State Street, Purdue University, West Lafayette, IN 47907 USA

[3]Department of Agronomy, 915 W. State Street, Purdue University, West Lafayette, IN 47907 USA.

[4]Department of Biological Sciences, 915 W. State Street, Purdue University, West Lafayette, IN 47907 USA

[5]Weldon School of Biomedical Engineering, 206 S. Martin Jischke Dr., Purdue University, West Lafayette, IN 47907 USA

*These authors contributed equally.

LobeFinder, a new convex hull-based cell phenotyping tool, detects and locates lobe positions in epidermal pavement cells.

39

42 Author contributions: D.M.U. and D.B.S. conceived the image analysis method. T.C.-W. and J.

43 P. wrote the LobeFinder code. S.B. generated the image data and evaluated the code. D.B.S.,

44 D.M.U., S.A.B., and T.C.-W. wrote the paper.

45

46 Abstract

47 Dicot leaves are comprised of a heterogeneous mosaic of jig-saw-puzzle piece shaped pavement

48 cells that vary greatly in size and the complexity of their shape. Given the importance of the

49 epidermis and this particular cell type for leaf expansion, there is a strong need to understand

50 how pavement cells morph from a simple polyhedral shape into highly lobed and interdigitated

51 cells. At present, it is still unclear how and when the patterns of lobing are initiated in pavement

52 cells, and one major technological bottleneck to address the problem is the lack of a robust and

53 objective methodology to identify and track lobing events during the transition from simple cell

54 geometry to lobed cells. We developed a convex-hull based algorithm termed LobeFinder to

55 identify lobes, quantify geometric properties, and create a useful graphical output for further

56 analysis. The algorithm was validated against manually curated cell images of pavement cells of

57 widely varying sizes and shapes. The ability to objectively count and detect new lobe initiation

58 events provides an improved quantitative framework to analyze mutant phenotypes, detect

59 symmetry-breaking events in time-lapse image data, and quantify the time-dependent correlation

60 between cell shape change and intracellular factors that may play a role in the morphogenesis

61 process.

62

63

Introduction

65

66   The size, shape, and angle of leaves are important adaptive traits in natural populations
67 and key determinants of yield in agronomic settings (Zhu et al., 2010). Therefore it is important
68 to understand the cellular events that collectively, at the levels of the tissues and organs, lead to
69 the formation of durable, lightweight, and appropriately sized leaf blades for efficient light
70 capture (Walter et al., 2009). In Arabidopsis, the growth properties of the epidermis may have
71 particular importance in terms of organ size control (Savaldi-Goldstein et al., 2007), and the
72 growth behaviors of the sectors of the epidermis and individual cells can correlate with
73 organ-level growth behaviors (Zhang et al., 2011; Kuchen et al., 2012). In dicots, the basic
74 cellular unit of the epidermis is the jig-saw-puzzle piece shaped pavement cell, the division and
75 expansion of which drive leaf expansion (Asl et al., 2011).

76   The biomechanics of pavement cell shape change are complicated (Panteris and Galatis,
77 2005; Szymanski and Cosgrove, 2009; Geitmann and Ortega, 2009; Szymanski, 2014). Turgor
78 pressure is the driving force for cell expansion. However, the magnitude and directions of cell
79 wall tension forces are difficult to predict because of the presence of adjacent neighboring cells
80 both in the plane of the epidermis and in the underlying mesophyll tissue (Szymanski, 2014).
81 The shape of the cell itself may also influence the stress patterns in the wall, and regions of high
82 cell curvature are predicted to have increased wall stress compared to other domains of the cell
83 (Sampathkumar et al., 2014). The growth trajectory or strain response of the cell is also strongly
84 influenced by heterogeneity in the cell wall, and a current challenge is to understand how
85 differences in cell wall thickness and local cellulose-dependent cell wall anisotropy might
86 contribute to polarized growth in this cell type (Panteris and Galatis, 2005; Szymanski, 2014).

87   The developmental control of lobe initiation in cotyledons and leaves is also poorly
88 understood. In one early model, lobe initiation was proposed to direct organ shape, with cell
89 elongation and lobe initiation occurring independently in populations of cells to influence organ
90 growth in length and width, respectively (Tsuge et al., 1996; Fu et al., 2002). Other studies,
91 which relied on cell shape measurements from populations of unsynchronized cells, detected
92 correlations between cell size and lobe number, implying a continuous process of cell expansion
93 and lobe initiation (Qiu et al., 2002; Fu et al., 2005). Neither of these models appears to be

94   correct based on several recent papers that employ either long-term time lapse imaging of

95   pavement cell morphogenesis (Zhang et al., 2011; Elsner et al., 2012) or cell population analyses

96   that analyzed cells from developmentally staged leaves over time intervals spanning days

97   (Andriankaja et al., 2012) or weeks (Staff et al., 2012). The clear outcome for these studies is

98   that the frequency of lobe initiation clearly depends on the developmental stage and location on

99   the leaf. However, in many instances lobe initiation is unpredictable. For example, a given cell's

100   anticlinal (perpendicular to the leaf surface) walls are in contact with several neighboring cells.

101   New lobes can form along either one or several of these cell boundaries, and the factors that

102   define the probability of forming a new lobe at a particular location are not known. Lobe

103   initiation is therefore episodic, and morphogenesis appears to include both anisotropic growth

104   during lobe initiation and lobe expansion, as well as extended phases of symmetrical cell

105   expansion in which the cell size increases but the overall geometry of the cell remains essentially

106   unchanged (Zhang et al., 2011).

107   One major limitation in the field is the lack of a robust and objective method to identify

108   new lobes. The discussion above on the cellular and developmental control of lobe formation is

109   largely based on subjective evaluation of pavement cell segments as being either lobed or

110   unlobed. This has generated confusion and variability in the literature with regard to detecting

111   phenotypes and comparing the severity of phenotypes among different mutants. In some

112   instances, the endpoints of a midline skeleton of individual pavement cells have been used to

113   estimate lobe number (Le et al., 2006; Staff et al., 2012); however, this method is not very

114   accurate and appears to underestimate lobe number. As an alternative, dimensionless shape

115   descriptors like circularity ($4\pi\Box cell\ area/perimeter^2$), a ratio that approaches 1 for more circular

116   cells and gets smaller as cells become more lobed, are used to test for differences among cells in

117   the complexity of their cell shape (Kieber et al., 1993; Le et al., 2003; Djakovic et al., 2006; Le

118   et al., 2006; Zhang et al., 2008). The major weakness of this approach is that it does not directly

119   reflect lobe number, and there are many equally plausible explanations in which reductions in

120   either lobe initiation or lobe expansion could lead to similar differences in cell shape complexity.

121   In this technical advance, we describe a highly useful convex hull-based Matlab program termed

122   LobeFinder that operates on cell perimeter coordinates extracted from images of pavement cells

123   and returns an array of useful cell shape data including a value of lobe number and a map of their

124   positions. Based on median scores of manually identified features from a diverse population of

125 pavement cells, LobeFinder predictions outperformed the alternative method of binary image

126 skeletonization and subjective human scoring. The development, validation, limitations, and uses

127 of LobeFinder are described below.

128

129

Results

Currently, quantification methods of lobe formation are often focused on the localization of specific factors related to cellular shape change such as the distribution of actin filaments, the presence of anticlinal microtubule bundles, and qualitative descriptions of cell shape (Fu et al., 2002; Fu et al., 2005). However, because there is no known marker protein for lobe initiation, and because lobe counting results vary greatly between labs and among individuals (see below), there is a strong need for a standardized computational approach to measure the number and location of pavement cell lobes.

A number of commercial and open-source software applications are available to quantify the geometry of cell shapes. These methods can be broadly separated into two categories: quantification of descriptive scalar properties such as circularity, roughness, perimeter, area, etc. that describe the shape by descriptive parameters (Russ, 2002; Robert et al., 2008); and image-segmentation approaches that we broadly define here as methods that reduce the pixel information in the raw image into segments or a reduced set of data points that have greater biological meaning (Marcuzzo et al., 2008), such as converting an image of a cell into segmented regions for nucleus, cytoplasm, golgi, ER, etc. automatically. These approaches offer a reduction in the size of the data and a transformation of pixel intensity data into classifications that directly informs the biology of the problem. The Medial Axis Transform (MAT) (Staff et al., 2012) has been used to quantify pavement cell geometry. The MAT uses the midline points of cells to quantify cell shape differences by tracking the percent change in angles between linear segments of the branches along the central axes or skeleton. A similar method for tracking the midline of a cell is available as the FIJI plugin AnalyzeSkeleton method (Arganda-Carreras et al., 2010; Schindelin et al., 2012).

In the analysis of pavement cell shape, the most widely used computational method to identify lobes is based on the AnalyzeSkeleton algorithm that detects the midline of irregularly shaped objects, categorizing the pixel properties of the surrounding area and choosing the best path to detect areas of image continuity. Based upon the number of neighboring pixels, some pixel points are ignored or favored over others and a skeletonized representation of the central axes of the cell's shape and structure is formed. In this method, individual cells are manually extracted from a confocal image of a field of pavement cells (Figure 1). A midline skeleton is

Skeletonized cell method
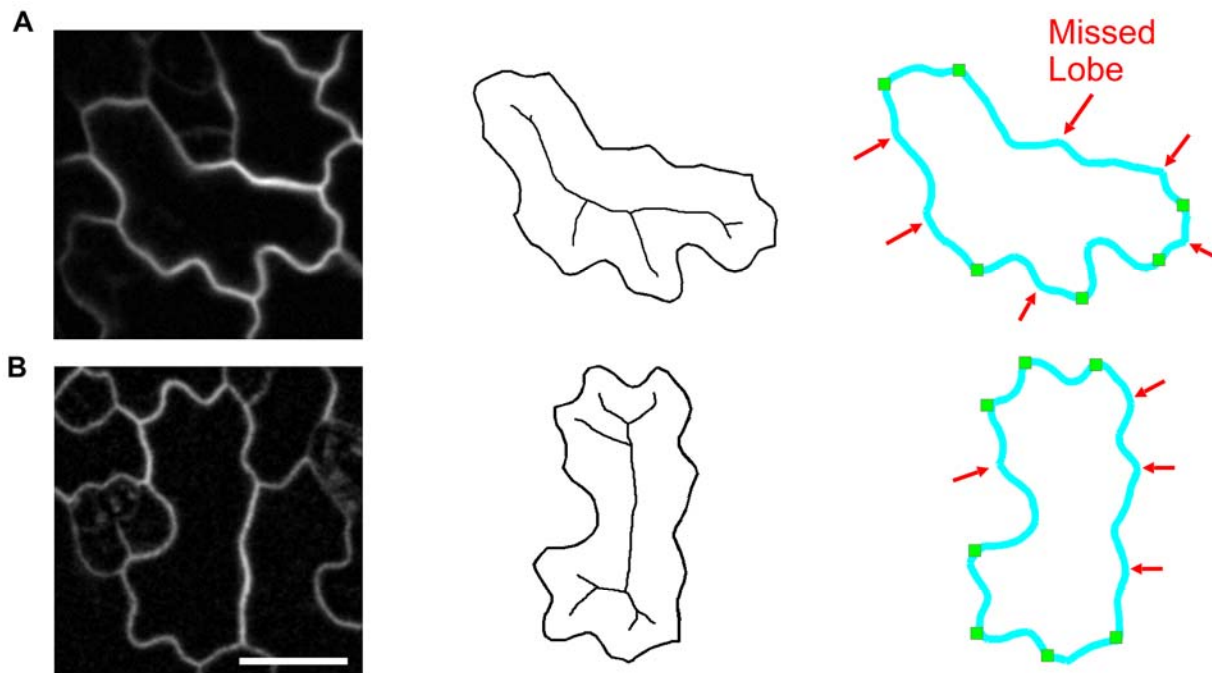
Figure 1. The AnalyzeSkeleton processing technique of lobe identification method does not accurately identify pavement cell lobes. **(A)** and **(B)**, Left, representative confocal images of an early stage cotyledon pavement cells. Middle, calculated midline skeletons of the corresponding pavement cells. Right, summary of the accuracy of the AnalyzeSkeleton method. Green squares, correctly identified lobe points based on the extensions of the skeleton endpoints; red arrows, missed lobe points compared to voting results. Scale bar, 20μm.

161 calculated from the binary image and the skeleton end-points are extended to the cell perimeter,

162 depending on the magnitude of the protrusion, to map positions of predicted lobes. As shown in

163 Figure 1A and Figure 1B, the skeletonize method is not very accurate, and only about half of the

164 lobes that would be identified by a trained scientist are accurately identified with this method.

165 Therefore, this method is useful in determining generalized lobing events, usually well after a

166 new lobe has formed, but is unable to detect slight variations in wall geometry that signify recent

167 lobing events.

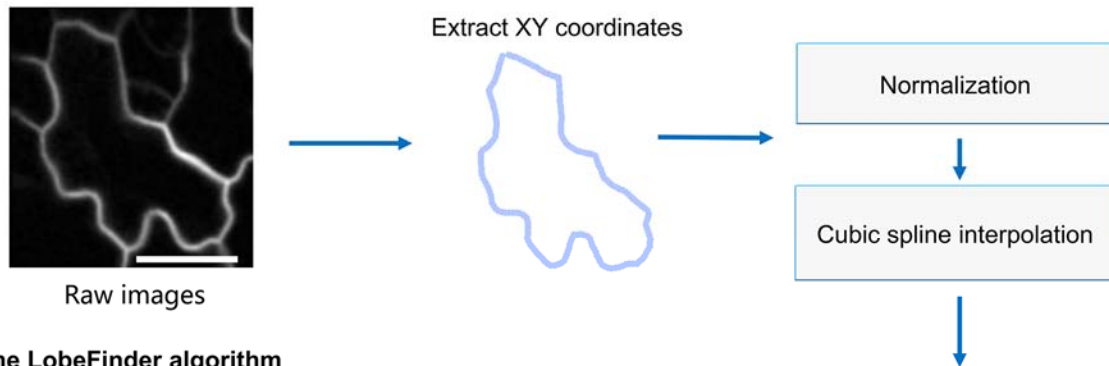168

169 *Outline of LobeFinder*

170   To overcome the limitations of the previous methods in identifying the position and

171 number of lobes in pavement cells, we developed a new cell geometry analysis approach named

172 LobeFinder. LobeFinder operates on user-supplied cell boundary coordinates that are extracted

173 from high-resolution confocal images of pavement cells of various sizes and shapes. The

174 algorithm is based on a multi-step process starting with a convex hull of the cell boundary and a

175 sequence of processing events to robustly identify lobes (Graham, 1972). First, cell boundaries

176 are segmented from the original image. For our analysis of cell boundary variation and lobe

177 detection, existing segmentation methods utilizing gradient vector field SNAKEs or a related

178 approach (Ma and Manjunath, 2000; Roeder et al., 2010) were not sufficiently accurate,

179 frequently merging cells or creating additional cells from an irregularly-shaped lobe. The

180 recently published semi-automated method for pavement cell segmentation termed CellECT

181 improves the efficiency of 3D pavement cell segmentation and includes user input to reduce

182 errors (Delibaltov et al., 2016). In the future, CellECT could be modified to output a single set of

183 splined coordinates that accurately depict the boundary of the anticlinal cell wall. We anticipate

184 that as cell segmentation methods improve, LobeFinder will be integrated into an image

185 processing workflow to enable high-throughput cell phenotyping. However, at the present time

186 manual segmentation is the only reliable method to extract cell coordinates, and this can be

187 easily achieved using the polygon selection tool that is available in ImageJ. The ImageJ

188 segmentation tool is advantageous because it allows the user to adjust the position of the cell

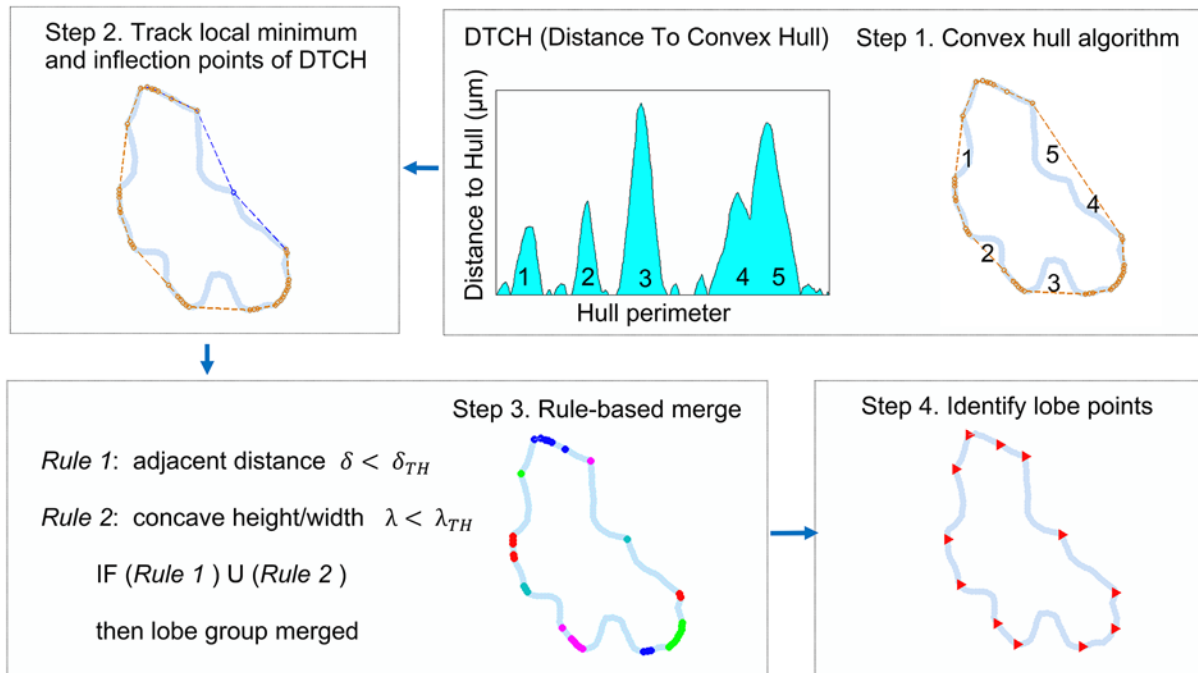189 boundary points and add or delete points as needed.

190 For this study, confocal images were at a resolution of 3.95 or 2.55 pixels/µm. After

191 testing a range of sampling densities along the cell perimeter, we found that sampling

192 frequencies of 0.5 to 1.5 points/µm were sufficient to yield accurate results for cell shape

193 analyses using LobeFinder because lobe detection was consistent in this range. Sampling

194 frequencies of 1 point every 2 µm or less led to obvious mismatches between the cell shapes in

195 the raw image and the segmented cells. We recommend sampling cell perimeters at 1 point/µm

196 and selecting the spline function within ImageJ to smooth the manual tracing and provide a high

197 density of interpolated points.

198 Following extraction of the cell perimeter by segmentation, the center of mass of each

199 cell is calculated and moved to the origin. The overall cell size is normalized and scaled by a

200 constant factor to calculate lobe numbers (Figure 2A). Following analysis the outputs are

201 rescaled back to microns for the outputs reported in the graphical user interface (GUI). This

202 allows the use of the same relative metrics and LobeFinder settings to determine if a lobe is

203 present for cells of different ages and sizes. The normalization step also allows raw images at

204 multiple different resolutions to be processed in LobeFinder. To remove artifacts introduced by

205 the uneven sampling of perimeter points during manual cell segmentation and reorientation, the

A Data preprocessing step

Raw images

Extract XY coordinates

Normalization

Cubic spline interpolation

B The LobeFinder algorithm

Step 2. Track local minimum and inflection points of DTCH

DTCH (Distance To Convex Hull)

Distance to Hull (µm)

Hull perimeter

Step 1. Convex hull algorithm

Step 3. Rule-based merge

Rule 1: adjacent distance $\delta < \delta_{TH}$

Rule 2: concave height/width $\lambda < \lambda_{TH}$

IF (*Rule 1*) U (*Rule 2*)

then lobe group merged

Step 4. Identify lobe points

Figure 2. Overview of the LobeFinder logic and workflow.
(A) Cell perimeter positions are manually segmented from raw images, scaled, and resampled.
(B) A convex hull, defined as the as the minimal polygon which encloses the entire given cell perimeter is computed (step 1), then the perimeter is scanned for missed lobe points (the extrema between segments 4 and 5) using the PeakFinder algorithm within MatLab (step 2). The optimized values for thresholds (δTH and λTH) (TH: Threshold) for rule based lobe geometry and spacing (step 3) are used to identify putative lobe points (step 3), and last, groups of lobe points are merged and the final set of predicted lobe positions are extracted (step 4). Scale bar, 20µm.

206   cell perimeter data is approximated by a cubic spline interpolation.

207   The output of the preprocessing steps is a cell perimeter that is scaled, aligned with the

208   center of mass, smoothed and resampled (cubic spline interpolation), and ready for further

209   analysis. To acquire the minimal polygon that surrounds the entire set of coordinates that define

210   the cell boundary (Figure 2B), we employ the MATLAB function 'convhull' that returns the

211 coordinates of the convex polygon (hull) that contains all the coordinate points of the cell set

212 (MATLAB, 2013). The convex hull provides two important features for further analysis: first it

213 provides information for the minimum convex set that encompasses the entire cell, and second it

214 provides a convenient coordinate system onto which the cell boundary properties are easily

215 mapped (Figure 2B, middle). Both of these outputs will serve to subsequently identify key points

216 and structures.

217   Pavement cells do not typically produce an outline where all of the extrema at the lobe

218 tips are located precisely on the hull. For example, in Figure 2B, the convex hull produces a line

219 that does not separate regions 4 and 5 by the lobe that is located between the regions since the

220 lobe does not land on the hull itself. To adjust the hull, the distance between the cell and the hull

221 is calculated and plotted on an axis of position vs. distance (Figure 2B). Using the orthogonal

222 Distance To the Convex Hull (DTCH) to the cell perimeter, the local minima are retrieved, and

223 the convex hull is then refined to capture the interior local minima points. To determine whether

224 there are interior lobe points between adjacent points on the convex hull, we use the program

225 PeakFinder (Yoder, 2011) to determine both local and absolute extrema between hull(i) and

226 hull(j) (points on the cell periphery coincident with hull). Peakfinder identifies the location of the

227 missed lobes and the hull used to encapsulate the cell is modified to contact the lobe point

228 (Figure 2B, step 2). These additional processing steps capture the majority of interior lobes that

229 would otherwise be missed since they do not lie on the hull surrounding each cell. The resulting

230 hull is termed the "refined hull" because it no longer conforms to the strict definition of a convex

231 hull. The Distance to the Refined Hull (DTRH) plots contain highly useful information on the

232 local patterns of growth. Therefore, the cell and its refined hull are re-scaled back to their real

233 dimensions, and the DTRH coordinates are available to be exported within the LobeFinder

234 program. In rare instances, there are relatively large pavement cells in which a cell lobe is

235 bulbous. In these instances the path of the cell perimeter doubles back on itself on one axis

236 creating multiple solutions for the DTRH plot. In this sub-region of the cell, the peakfinder

237 routine uses only the smallest distance value, and this can lead to erroneous hull refinements and

238 lobe calls. This morphology is rare in our dataset, but a bulbous morphology is the default state

239 in the crenulated boundary of many monocot leaf epidermal cells. For these species, LobeFinder

240 would likely perform well in analyzing early events associated with lobe initiation, but would

241 likely fail to accurately count the lobes of fully expanded cells.

242   Following adjustment of the convex hull, the goal of the algorithm is to identify which of

243   the points on the cell perimeter correspond to the positions of the protrusions. Additionally, not

244   every point on the hull corresponds to a physical lobe on the pavement cell, and to some extent

245   the identification of a lobe on the cell is subjective in nature with different individuals

246   identifying different lobe positions and numbers. One design goal of the algorithm is to mimic

247   the expert observer's approach to identify the geometric features, albeit by an objective computer

248   algorithm. This goal informed the design of the geometric parameters for lobe geometry and

249   spacing that were developed to optimize lobe identification. For each data point in the set of

250   convex hull points (Figure 2B, Step 3), the distance between neighboring points is calculated.

251   This distance between hull points determines if the algorithm should consider adjacent lobe

252   points as part of the same lobe. To cull points on the hull and leave only those that are identified

253   as the center of a lobe, two parameters (δ and λ) for the initial identification of lobes are used:

254   the scaled spacing distance between lobe points (δ), and a ratio of the height (distance between

255   hull and cell boundary) to the width (distance of hull segment) between prospective lobe points

256   (λ). The distance between a lobe point and the convex hull is zero, however there must be a

257   region between lobes where the distance is non-zero and above some threshold value. This

258   module of the program calibrates LobeFinder to reduce the number of misleading or incorrect

259   lobe points on the convex hull. This calibration is effective in most cases. However, because the

260   parameters are tuned to be sensitive for small deviations in boundary shape, cells with relatively

261   simple shapes with extended domains of the cell boundary that are close to the the threshold

262   values for δ and λ are most likely to have false positives.

263

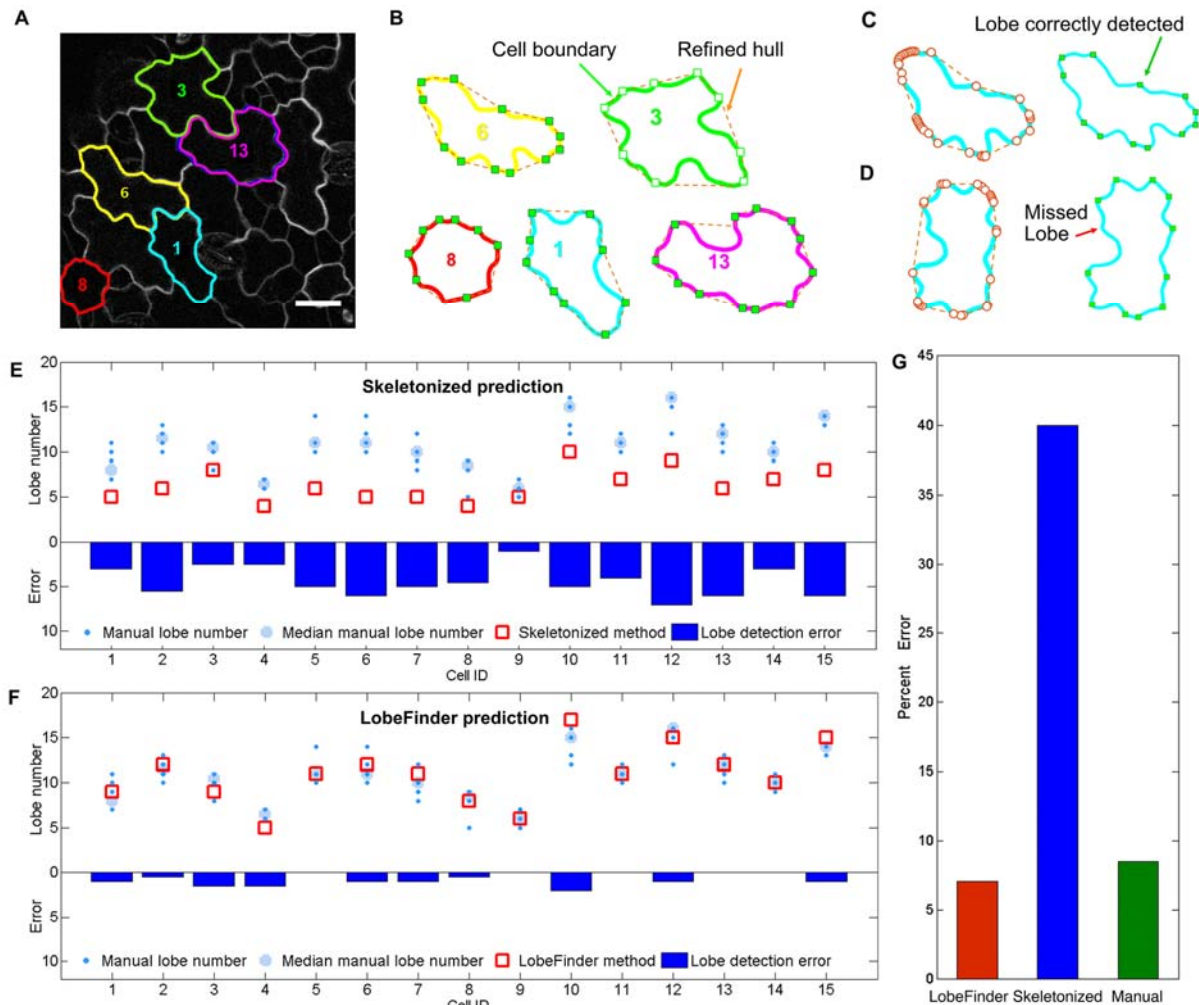264   LobeFinder *optimization and evaluation*

265   The principal method for identification of lobes and lobing segments in pavement cells

266   relies on observer-based inspection and identification of lobing events. An important research

267   goal is to standardize pavement cell phenotyping and to create an objective computational

268   method that can accurately quantify cellular geometry and be applied to time-lapse data and large

269   ensembles of images to efficiently calculate population statistics. It is therefore necessary to

270   ensure the algorithm produces consistent and accurate observations.

271   As an initial test of the sensitivity of the output to variability in an individual's choice of

272   boundary points for cell segmentation, three pavement cells of varying sizes and shapes were

manually segmented three times and analyzed using LobeFinder. For each of these cells the area, perimeter, and circularity values for the technical replicates were either identical or differed by a fraction of a percent. For the technical replicates the LobeFinder outputs for lobe number were more variable, with the coefficients of variation for lobe number varying between .06 and .10. This level of variabilty in the measurement of lobe number was much less than that observed when multiple individuals used subjective criteria to score an identical cell. For example, in our test population of pavement cells (Supplementary Figure S1), the coefficient of variation for lobe number ranged from 0.03 to 0.21, with 10 of the 15 cells having a coefficient of variation greater than 0.1. In the LobeFinder program, variability in lobe number most often occurred along relatively straight cell perimeter segments with one tracing including a very small feature that was absent in another. The cause for this is discussed further below, but this result makes clear the importance of accurate sampling along the cell perimeter.

Fifteen randomly selected pavement cells (Supplemental Figure S1) from a time-lapsed dataset were used to more thoroughly compare the accuracy of LobeFinder compared to exisiting methods. The cells had sizes that ranged from 280 to 1588 μm^2, and circularity values that ranged from 0.32 to 0.81. We evaluated how well LobeFinder outputs of lobe number and lobe position would agree with the scores generated by researchers with experience in the analysis of pavement cell shape. For each of the images (examples shown in Figure 3), six experienced pavement cell scientists visually inspected 8.5" X 11" printouts of each cell and identified lobe locations for each raw image. These data were used to determine the accuracy of lobe point position detection and to calculate the number of lobes present for each cell (Figure 3C and Figure 3D). A few of the cells used in the calibration of LobeFinder are shown in Figure 3A. The complete set of images (Supplemental Figure S1), and a summary of the cell and convex hull properties (Supplemental Table 1) are provided in the supporting online materials. A summary of the LobeFinder and voter results are shown in Figure 3E and Figure 3F. We next benchmarked LobeFinder and the existing skeletonize method against the images manually curated by members of the two labs. The subjective nature of the manual scoring of lobe number is evident in the plots of lobe number (Figure 3E and Figure 3F), with many cells having four or more features that were ambiguous. The median lobe number from the manually curated data was therefore used as a standard for comparison.

Overall, the skeletonize method greatly underestimated lobe numbers (Figure 3E).

Figure 3. Evaluation of the LobeFinder accuracy using a calibration dataset and parameter optimization. **(A)** Example of a raw image containing five cotyledon pavement cells in the calibration dataset. **(B)** Outlines of extracted cells showing the cell boundary and the unrefined convex hull. **(C, D)** Example output of LobeFinder for two cells in which the correctly identified (green squares) and missed (red arrow) lobes are marked. **(E)** Comparison of the skeletonize method with manually curated results. The light blue circles are the median values from manual lobe identification results for each cell with individual independent values in small dark blue dots, and red boxes are lobe numbers predicted by skeletonize method. The dark blue bars plot are the absolute value of the difference between the lobe number count from the skeletonize method and the median value from the manual results. **(F)** Comparison of the LobeFinder method with manually curated results. The symbols and bars are as described in **(E)**, but here the red boxes are the lobe numbers predicted by LobeFinder. The dark blue bars are the absolute value differences between the lobe number count from LobeFinder and the median value from manual results. **(G)** Comparison of the percent errors of the LobeFinder, skeletonize, and manual scoring methods that were calculated using the median lobe number as the correct value for each cell. Scale bar, 20µm.

304   Following an initial calibration to optimize the threshold values of   and☐ , the LobeFinder

305   outputs for lobe number closely matched the median lobe numbers from the manually curated

306   images (Figure 3F). The LobeFinder lobe number error was 5.7 times lower than that of the

307   skeletonize method (Figure 3G). The accuracy of the manual lobe counts were similar to those of

308   LobeFinder when averaged across all individuals (Figure 3G); however for a given cell there was

309   considerable spread in the lobe counts among the individuals (Figure 3F). For example, the error

310   rate among the individuals differed by more than 20% for 8 of the 15 cells, even though each of

311   the 6 individuals were similarly-trained to score the presence of lobes. This observation

312   reinforces the strong need for objective methods for quantitative analysis of cells with highly

313   variable shapes and sizes.

314   Two different types of features were typically identified as a lobe. First, there were

315   instances of an undulation along a cell perimeter segment that were independent of a 3-way cell

316   wall junction. This is the classic example of interdigitated growth among two adjacent cells, and

317   we define these features as Type I lobes. A second class of cell protrusions, defined here as Type

318   II lobes, were instances in which a protrusion was located at a 3-way cell wall junction. These

319   tripartite junctions form during cytokinesis, and in some, but not all cases, the cell can grow

320   asymmetrically at this location generating a protrusion with a shape that is often

321   indistinguishable from Type I lobes. However, the growth mechanism that generates a Type II

322   lobe may resemble "intrusive" growth (Jura et al., 2006) in which one cell expands

323   asymmetrically at the interface of two adjacent cells. This form of asymmetric growth likely

324   differs from that which generates lobes that are independent of tripartite junctions. There is

325   certainly a need to distinguish between these different types when one analyzes phenotypes and

326   gene function. Currently, this is a weakness of LobeFinder because the program operates on the

327   coordinates of individual cells and information on the cell wall patterns of its neighboring cells is

328   lost. At present, if a user wishes to distinguish Type I and Type II lobes, one can use the

329   graphical output from LobeFinder to identify the subset of lobes that fall on 3-way cell wall

330   junctions. In the future, we hope to use a semi-automated cell segmentation program like

331   CellECT (Delibaltov et al., 2016) to simultaneously extract cell coordinates from fields of cells

332   and track the positions of 3-way cell wall boundaries.

333   To quantitatively evaluate the performance of the algorithm for lobe location, we

334   compared the position of the predicted lobes against the manually determined lobes within a

335   specified tolerance (0.025 radians). If LobeFinder identified the proper location within the

336   tolerance, it is identified as a true positive (TP, Supplemental Figure S2). If a predicted

337   LobeFinder point was not within 0.025 radians of a manually identified point, it was considered

338 a false positive (FP). Missed Lobe points were defined as false negatives (FN). We did not

339 calculate true negatives since this would be an ambiguous number to determine and it would not

340 inform the evaluation of the method. Related to these quantities, we also calculated the

341 Sensitivity = TP/(TP+FN) and False Discovery Rate (FDR) = FP/(TP+FP). Both of these

342 measures are used to determine the effectiveness of the algorithm.

343   A high sensitivity and a low FDR are the primary objectives for the application of

344 LobeFinder as a tool for reliable and automated measurement of cell shape properties. Nine

345 different combinations of the parameters   and□   were tested that covered a wide range of

346 parameter values. The highest parameter values yielded decreased senstivity and increased false

347 positives; however, there was a fairly broad range of parameter combinations that yielded a

348 sensitvity of ~0.8 and an FDR of ~0.25 (Supplemental Figure S2). This indicates a relatively low

349 dependence of the algorithm on the specific parameters. The optimized parameter combinations

350 yielded an average sensitivity of 0.95 or higher and an average FDR less than 0.2 (Supplemental

351 Figure S2).

352

353 *Identification of new lobes in time-lapse images of pavement cells*

354 The lobe number, shape, and size properties of pavement cells were analyzed on populations of

355 cells at different intervals of cotyledon development. We applied the LobeFinder program to

356 identify lobes in three time-lapse datasets of pavement cell growth. The first dataset represents

357 early growth from 38 hours after germination (HAG) to 56 HAG. This slightly overlaps with the

358 second dataset from 48 HAG to 120 HAG. The third dataset covers 72 HAG to 120 HAG.

359 Datasets 2 and 3 were part of a previous analysis of pavement cell growth (Zhang et al., 2011),

360 and the raw images were reanalyzed here using LobeFinder. Example cells from these three

361 different datasets are shown in Figure 4A to Figure 4C. Each showed combinations of

362 symmetrical lateral expansion, with datasets 1 and 2 including more cells that initiated new lobes

363 during the time interval. For example, the cell that is representative of the 72-120 HAG dataset,

364 we observed no change in lobe number over the course of time, but it increased in size (Figure

365 4C, left to right). In contrast, the image representing a cell in the 48-120 HAG dataset initiated

366 five new lobes (Figure 4B, left to right) while the image in the 38-55 HAG added three new

367 lobes in the timespan of 27 hours (Figure 4A, left to right). There is a great deal of variability in

368 pavement cell size and lobe number as a function of cotyledon and leaf development (Elsner et
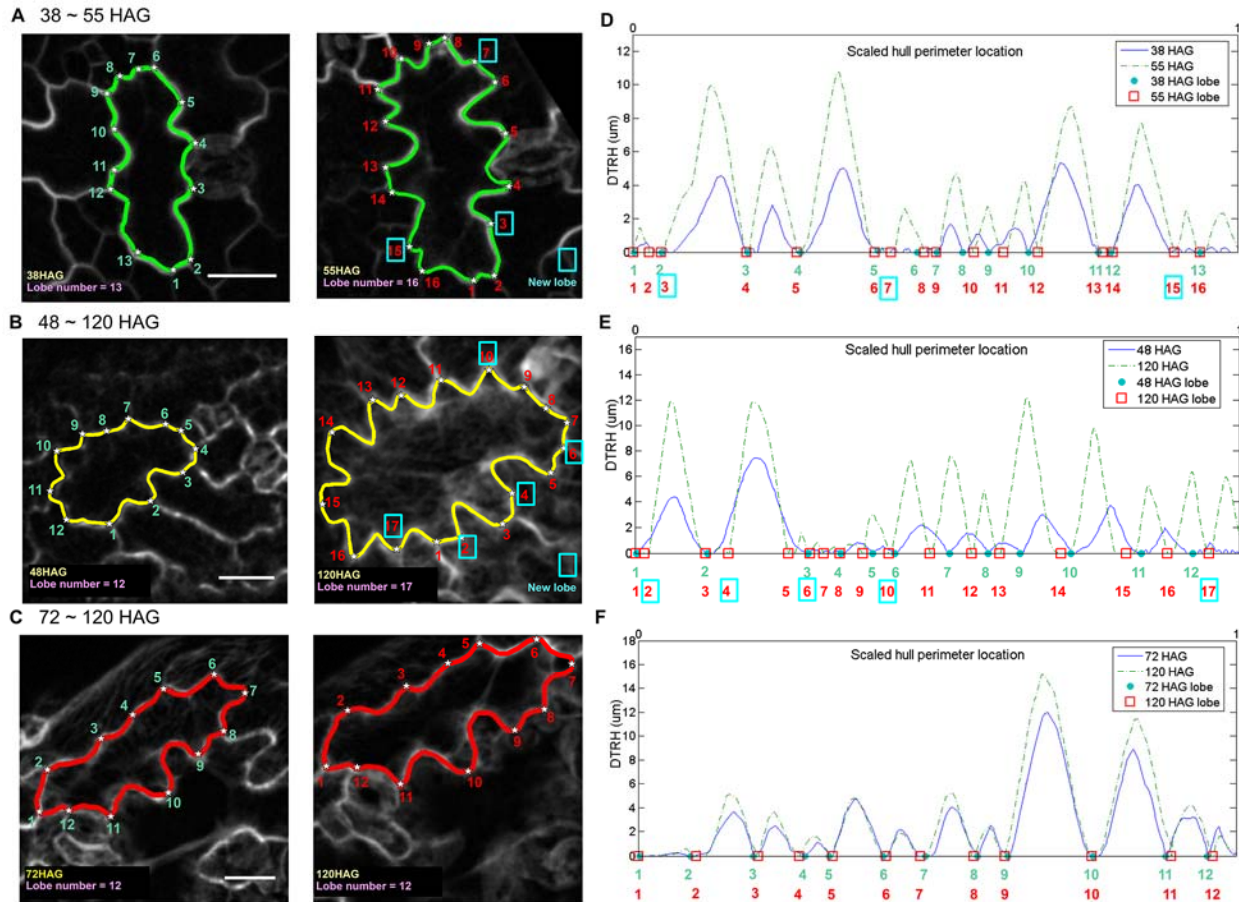
Figure 4. LobeFinder can be used to detect new lobes and quantify growth patterns in time-lapse images. **(A-C)**, Examples of raw images of pavement cells with manually segmented cell shapes at three different intervals of cotyledon development. **(A)** Pavement cell at 38 (left) and 55 (right) HAG. **(B)** Pavement cell at 48 (left) and 120 (right) HAG. **(C)** Pavement cell at 72 (left) and 120 (right) HAG. The blue boxes indicate the detection of new lobes and their location in the images and on the DTRH plots. **(D-F)** The DTRH plots for pavement cells that were re-scaled to their original size. The x-axes of these plots are the scaled distance along the convex hull perimeter at the two different time points to enable visual comparisons of similar relative positions along the cell boundary at the two time points. The blue line is the DTRH at the initial time-point and dotted green line is DTRH at the final time-point. The time points in D to F, correspond to those of A to C, respectively, and are shown in the legend for each of the plots. The blue dots and red boxes on the x-axis identify lobe locations in the initial and final time points, respectively. Scale bar, 20μm.

369   al., 2012; Staff et al., 2012). As a result, in the relatively small windows of time that are analyzed

370   here, there are examples in which lobe number and cell area are not strictly correlated with

371   developmental time (Table 1, Supplemental Table 1). However, differences in lobe initiation

372   rates of individual cells within the time intervals were apparent. Overall, the average number of

373   new lobes per cell was about 2.5 for the 38-55 HAG and 48-120 HAG populations, and 0.5 for

374   72-120 HAG (Table 1). The percentage of cells in all datasets that grew new lobes, were 33

375   percent for 72-120 HAG, 93 percent for 48-120 HAG, and 80 percent for 38-55 HAG (Table 1).

17

376 These LobeFinder outputs and the average number of lobes per cell at each time point (Table 1)
377 indicate that lobing events are prevalent in early stages of growth, and that lobing events slow
378 down at some point between 56 and 72 HAG. These results are consistent with the conclusions
379 of a previous study (Zhang et al., 2011).

380 Additional scalar metric outputs from LobeFinder also correlate with different phases of
381 pavement cell growth; however, they do not directly inform the generation of new lobes.
382 Specifically, for example, the circularity of the individual cells decreases between the two time
383 points (Table 2), likely due to the increased expansion of lobes that are initiated primarily in the
384 first two and half days after germination. This would also explain the observed decreases in the
385 convexity (ratio of hull perimeter to cell perimeter) and solidity (ratio of hull area to cell area) of
386 pavement cells. Overall, the identification of lobing events and the scalar metrics are consistent
387 with the existence of a permissive developmental window for active lobe formation early in
388 cotyledon development.

389 Another outputs from LobeFinder that are useful for cell analyses are plots of the distance
390 from the refined hull to the cell boundary, which provide a graphical representation of the
391 magnitudes and directions of cell shape change near the cell periphery. This is due to the fact that
392 as lobes expand, their height and width increase leading to corresponding changes in the DTRH
393 plots.   At the distal tips of cell protrusions, the DTRH is zero and corresponds to a lobe point of
394 the cell of interest in the LobeFinder output. The shape of the cell boundary between lobes is
395 captured by the contour of the DTRH, which is at a local maximum at the most concave position
396 between lobes. Therefore, in a time lapse experiment, the DTRH plots reflect the local growth
397 behavoirs of the adjacent protruding cell, and the shape change at the interface between the two
398 cells. In Figure 4D to Figure 4F, the DTRH was plotted for each cell at the two different time
399 points. The position along the hull is the x-axis, and this is scaled to the hull length of the initial
400 time point to enable the DTRH values from different time points to be compared at similar
401 relative positions along the hull perimeter. During the 72 to 120 HAG interval (Figure 4F),
402 growth is highly symmetrical and lobe initiation is rare (Zhang et al., 2011). The corresponding
403 DTRH plots were consistent with this result, because the contours of the plots at the two time
404 points were highly symmetrical with well-aligned peaks. It is important to note that the peak
405 widths for the later time points are compressed because the x-axis is scaled. However, as
406 previously shown (Zhang et al., 2011), pavement cell growth during this phase is not perfectly

407   symmetrical, and there were sub-regions of the DTRH plots that were not symmetrical (Figure

408   4F), indicating that some local warping of cell shape occurred during growth. The paired DTRH

409   plots for cells that form new lobes (Figure 4E and Figure 4F), reflected a composite growth

410   behavior. In some regions of the cell-cell interface growth appeared symmetrical with

411   proportional increases in peak height and width at similar relative positions. The DTRH plots

412   also revealed an obvious contribution of polarized growth to the shape change, because new

413   peaks were detected. In addition, many of the peaks were shifted in position along the hull

414   perimeter, reflecting symmetry breaking during lobe initiation and accumulation of local warping

415   during the growth interval.

416

417

Discussion

418

419 LobeFinder is a novel convex hull-based tool to quantify the local boundary

420 characteristics of a closed geometric shape and identify key features such as pavement cell lobes.

421 The ability of LobeFinder to consistently and accurately identify and position lobes within a

422 pavement cell is an important advance, because currently there is no reliable method to quantify

423 the convoluted shape of pavement cells. Manual definition of lobe number (Fu et al., 2005; Xu et

424 al., 2010) or a feature such as the pavement cell neck-width (the shortest distance across the cell

425 between two indentations) (Lin et al., 2013) is subjective and variable. Variation in human

426 scoring is a major problem: we document here significant variability in lobe number scoring,

427 even among well-trained individuals (Figure 3E and Figure 3G). The lack of standardized

428 phenotyping methods can contribute to differing conclusions as to whether or not a particular

429 mutant has a pavement cell phenotype (Xu et al., 2010; Gao et al., 2015). Manual cell scoring is

430 also time-consuming. It requires careful inspection of the cell boundary and the manual

431 annotation of each feature in the image file that is scored as a lobe. Skeletonization of

432 segmented, binary images of cells can identify pavement cell protrusions (Staff et al., 2012), and

433 in some instances can be used to detect significant differences between mutant and wild type

434 plants (Le et al., 2006). However, the skeletonize technique is very inaccurate and tends to miss

435 approximately 40% of all lobes (Figure 3G). LobeFinder has a much greater accuracy compared

436 to the skeletonize method, and performs with an accuracy that is only achieved by averaging the

437 votes of several individuals with extensive experience in pavement cell analysis (Figure 3G).

438 The availability of an accurate method to directly identify pavement cell lobes is

439 important because scalar shape descriptors such as circularity are sensitive to multiple features of

440 a cell geometry, and do not contain information on the local cell features that are most useful for

441 understanding cell growth behavior. For example, differences between cells in their scalar

442 descriptors could reflect either differences in lobe number, reduced lobe expansion, or altered

443 diffuse growth in the mid-region of the cells. This point is important because it is often assumed

444 that any mutant with a reduced perimeter to area ratio has a lobe initiation defect. LobeFinder

445 directly analyzes the local geometry of the cell and identifies lobes. In this regard, it is a

446 powerful phenotyping tool that can be used to compare populations of cells and cell shape over

447 time. However, the LobeFinder program is not perfect, and because of the local shape and

448 spacing thresholds that are used for lobe detection, there are instances, most often along extended

449 domains of low curvature, in which false positives are occasionally reported. Overall,
450 LobeFinder has great potential for the community, and we anticipate that LobeFinder, provided
451 as a user-friendly program in MatLab (Supplmental Figure S3), will allow others to use this
452 program to analyze mutants, and objectively test for direct effects on lobe initiation.

453   A major advantage of LobeFinder is that it creates a coordinate system to quantify local
454 growth behaviors at the interface of two cells. Alternative approaches to lobe detection, such as
455 the quantification of the local curvature of the cell perimeter using variation in the tangent to the
456 cell boundary as a function of cell perimeter, could operate on splined images to identify regions
457 of local curvature that accurately identify lobes. However, this strategy would not generate a
458 coordinate system to analyze growth. Here we use LobeFinder and plots of the DTRH in time
459 series data to illustrate a method to quantify local growth behaviors of an irregularly shaped cell
460 (Figure 4). For example, the DTRH plots could be analyzed further in time-lapse experiments to
461 generate spatial maps of how the magnitude and direction of growth at the interface of two cells
462 change. These plots clearly indicate the timing, location, and pattern of polarized growth along
463 the interface of interdigitating pavement cells. Importantly, these plots do not reveal the
464 subcellualr patterns of growth that explain the shape change. To solve this problem, convex-hull
465 based growth analysis coupled with the use of fiducial marks on the cell wall to track growth
466 patterns (Zhang et al., 2011; Elsner et al., 2012; Staff et al., 2012) could provide improved
467 methods to analyze the subcellular heterogeneity in polarized growth. While this paper was being
468 written, there was a recent report in which externally applied particles were used to track the
469 growth patterns of the outer wall in fields of developing pavement cells (Armour et al., 2015).
470 The utility of externally applied particles to analyze the growth of the anticlinal wall is uncertain.
471 However, the combined use of DTRH plots, high-density cell wall marking, and time lapse
472 imaging has the potential to reveal how the polarized growth of individual cells and cell clusters
473 can operate at broader spatial scales to dictate the growth patterns of leaf sectors and even whole
474 organs (Zhang et al., 2011; Kuchen et al., 2012; Remmler and Rolland-Lagan, 2012).

475   LobeFinder also has immediate applications in terms of more quantitatively dissecting
476 the molecular control of lobe initiation. Hull based methods and the DTRH plots establish a
477 perimeter coordinate system onto which the temporal and spatial patterns of lobe formation can
478 be graphed (Figure 4). This is a boon for further analysis such as correlation of spatial
479 geometric features with the localization of cell wall and intracellular signaling and structural

480   factors that are believed to control symmetry breaking. Specifically, LobeFinder can provide the

481   convex hull coordinate system to test for correlations between the local accumulation of proteins

482   such as auxin efflux carriers (Fu et al., 2005; Xu et al., 2010) or microtubules (Panteris et al.,

483   1993; Qiu et al., 2002; Panteris and Galatis, 2005; Ambrose et al., 2007; Kirik et al., 2007;

484   Zhang et al., 2011) and lobe initiation. In this manner, an array of GFP-tagged proteins can be

485   tested to determine those whose localization and activity at the cell cortex specify

486   symmetry-breaking events.

487   Currently, the greatest limitation for LobeFinder is that it operates on cell coordinates

488   from manually segmented cells. Manual segmentation is a reliable, but time consuming process,

489   presenting a major bottleneck for high-throughput phenotyping. As discussed previously, the use

490   of individual, segmented cells also makes it impossible to distinguish between Type I and Type

491   II lobes, which complicates one's ability to test for alterative genetic control mechanisms and

492   differing contributions of the lobe types to cell expansion. The obvious solution is an automated

493   cell segmentation program that accurately extracts cell boundary coordinates and marks 3-way

494   cell wall junctions in the dataset. Currently, there is no existing segmentation method to

495   accurately extract pavement cell coordinates from fields of cells and track 3-way junctions.

496   However, the development of watershed-based cell segmentation coupled with user-guided

497   validation in a program like CellECT (Delibaltov et al., 2016) has the potential to be integrated

498   with LobeFinder to create a more robust and efficient cell analysis pipeline.

499   We show here that LobeFinder is an effective new tool for pavement cell phenotyping

500   and growth analysis. We believe this algorithm has a broader utility for the quantification and

501   many lobed cell types (Panteris and Galatis, 2005) and the analysis of objects with closed and

502   highly irregular geometric shape at any spatial scale. For example, there is great interest in the

503   quantitative analysis of leaf shape, and the complex boundary shapes of many types of leaves

504   could be analyzed with LobeFinder. In this context, LobeFinder, could complement other leaf

505   shape analysis programs like LeafProcessor (Backhaus et al., 2010). Similar hull-based methods

506   could operate on projected images of shoots and roots to analyze whole plant architecture over

507   time. We also believe LobeFinder could have broad applications in other fields such as human

508   medicine and environmental science. For example, the progression of irregularly-shaped tumors

509   could be quantified over time, and correlated with other features such as tumor location or drug

510   treatment regimes. The local spatial dynamics of spreading plumes of contamination, floods, and

511 the retraction of glaciers could be similarly analyzed, and tested for cross-correlations with any
512 variable of interest. Our efforts will focus on the use and integration of LobeFinder within a
513 completely automated image analysis platform, with the goal of accelerating discovery in the
514 field of leaf morphogenesis.

515

516

517 **Materials and Methods**

518 **Annotation and use of the LobeFinder program**

519 To run LobeFinder, start an instance of Matlab ® on the workstation (PC, MAC, Linux) and
520 change the working directory to the install location of LobeFinder. The script and all functions
521 that make up LobeFinder are located in one Matlab ® m-file: 'LobeFinder_GUI.m'. To run
522 LobeFinder, first create a directory to which all region-of-interest (ROI) of cell perimeter
523 coordinates obtained by manual segmentation are saved. Start the LobeFinder Graphical User
524 Interface (GUI) by typing 'LobeFinder_GUI' at the MATLAB workspace prompt and <Enter>.
525 This will open an instance of LobeFinder GUI in a separate window (Supplemental Figure S3).
526 To import files, click on the "Open Folder" button to select the folder that contains the ROI files.
527 At this point one can select the checkboxes for the types of data output files to be generated
528 (CSV, Figures, Matlab File) as well as the resolution of the images from which the ROIs were
529 extracted. Once the folder and options have been selected, click on the "Run" button to start the
530 ROI processing. The total number of ROI files being processed will be shown in the image
531 number box on the GUI. To view the results from the LobeFinder processing, select the image
532 number from the image number box. This will populate the GUI with the measured parameters
533 as well as an image of the refined hull, the cell boundary, identified lobe points, and DTRH plot.
534 Moving the cursor over the perimeter of the cell will allow its corresponding position on the
535 DTRH plot to be seen. Depending on the output options selected, a new folder in the directory of
536 LobeFinder will be created ([Output]_NameOfInputFolder) with up to 3 folders (CSV, FIG_cell,
537 FIG_dtrh). CSV folder contains one Matlab mat-file 'Lobe_result.mat' which contains all results
538 and geometric scalar properties for each ROI in the directory, a 'CellDescriptors.csv' file
539 containing all single value measurements such as area, perimeter, etc for all ROIs, and individual
540 'DTRH_[nameOfROI] file containing xy-values for DTRH plots. FIG_cell and FIG_dtrh folders
541 will contain images of cells and DTRH plots as displayed in the LobeFinder GUI.

542 ROILobeFinder is available for download at the Dryad Digital Repository:

543 http://doi.org/10.5061/dryad.cs78t

544 **Plant material and growth conditions.**

545 Arabidopsis seeds were grown on 1/2X Murashige and Skoog medium with 1 percent sucrose

546 and 0.8 percent Bacto agar under constant illumination at 22^0C. Seeds were treated with a 6 hr

547 light pulse, cold-treated for 3 days, then placed in the growth chamber. Germination was checked

548 36 hrs after plating, and only seedlings with a barely visible radicle were used for further

549 analysis.

550 **Time-lapse imaging of lobe initiation.** For time point imaging, cell outlines were detected using

551 a tubulin:GFP marker for datasets 2 and 3 as previously described (Zhang et al., 2011). For

552 dataset 1, from 38 to 55 HAG, 10 cells were analyzed. For dataset 2, from 48 to 120 HAG 12

553 cells were analyzed. For dataset 3, from 72 to 120 HAG 12 cell were analyzed. For dataset 1, the

554 PIN7:GFP (Blilou et al., 2005) plasma membrane marker was used. The seedlings were mounted

555 in water using a petroleum jelly gasket to form a chambered microscope slide. After initial

556 imaging, the slides were returned to the growth chamber until the next imaging session. Samples

557 were imaged using a Bio-Rad 2100 laser scanning confocal microscope mounted on a Nikon

558 eclipse E800 stand. Images were obtained with a 60X 1.2 NA water objective. Samples were

559 excited with a 488 nm laser and fluorescence signal was collected using a 490 nm long pass

560 dichroic, and a 500-550 nm band-pass emission filter. Selected planes from confocal image

561 stacks were converted to maximum intensity projects and were traced with the polygon selection

562 tool using in FIJI 4.0 (Schindelin et al., 2012). The coordinates from the ROIs from the manually

563 segmented cells were used as the input for LobeFinder.

564

565 Supplemental Data

566 Supplemental Figure S1. Examples of raw confocal images of pavement cells and

567 skeletonization results for the 15 cells that were used to validate LobeFinder.

568 Supplemental Figure S2. Sensitivity and accuracy analysis of LobeFinder performance.

569 Supplemental Figure S3. Snapshot of the graphical user interface of LobeFinder

570 Supplemental Table 1:   Morphological properties of pavement cells measured using

571 LobeFinder.

572

573

574

FIGURE LEGENDS

576

Figure 1. The AnalyzeSkeleton processing technique of lobe identification method does not accurately identify pavement cell lobes.

(A) and **(B)**, Left, representative confocal images of an early stage cotyledon pavement cells. Middle, calculated midline skeletons of the corresponding pavement cells. Right, summary of the accuracy of the AnalyzeSkeleton method. Green squares, correctly identified lobe points based on the extensions of the skeleton endpoints; red arrows, missed lobe points compared to voting results. Scale bar, 20μm.

584

Figure 2. Overview of the LobeFinder logic and workflow.

(A) Cell perimeter positions are manually segmented from raw images, scaled, and resampled. **(B)** A convex hull, defined as the as the minimal polygon which encloses the entire given cell perimeter is computed (step 1), then the perimeter is scanned for missed lobe points (the extrema between segments 4 and 5) using the PeakFinder algorithm within MatLab (step 2). The optimized values for thresholds (δ_{TH} and λ_{TH}) (TH: Threshold) for rule based lobe geometry and spacing (step 3) are used to identify putative lobe points (step 3), and last, groups of lobe points are merged and the final set of predicted lobe positions are extracted (step 4). Scale bar, 20μm.

593

Figure 3. Evaluation of the LobeFinder accuracy using a calibration dataset and parameter optimization. **(A)** Example of a raw image containing five cotyledon pavement cells in the calibration dataset. **(B)** Outlines of extracted cells showing the cell boundary and the unrefined convex hull.**(C, D)** Example output of LobeFinder for two cells in which the correctly identified (green squares) and missed (red arrow) lobes are marked**. (E)** Comparison of the skeletonize method with manually curated results. The light blue circles are the median values from manual lobe identification results for each cell with individual independent values in small dark blue dots, and red boxes are lobe numbers predicted by skeletonize method. The dark blue bars plot are the absolute value of the difference between the lobe number count from the skeletonize

603   method and the median value from the manual results. **(F)** Comparison of the LobeFinder

604   method with manually curated results. The symbols and bars are as described in (E), but here the

605   red boxes are the lobe numbers predicted by LobeFinder. The dark blue bars are the absolute

606   value differences between the lobe number count from LobeFinder and the median value from

607   manual results. **(G)** Comparison of the percent errors of the LobeFinder, skeletonize, and manual

608   scoring methods that were calculated using the median lobe number as the correct value for each

609   cell. Scale bar, 20μm.

610

611   **Figure 4.** LobeFinder can be used to detect new lobes and quantify growth patterns in time-lapse

612   images. **(A-C)**, Examples of raw images of pavement cells with manually segmented cell shapes

613   at three different intervals of cotyledon development. **(A)** Pavement cell at 38 (left) and 55

614   (right) HAG. **(B)** Pavement cell at 48 (left) and 120 (right) HAG. **(C)** Pavement cell at 72 (left)

615   and 120 (right) HAG. The blue boxes indicate the detection of new lobes and their location in the

616   images and on the DTRH plots. **(D-F)** The DTRH plots for pavement cells that were re-scaled to

617   their original size. The x-axes of these plots are the scaled distance along the convex hull

618   perimeter at the two different time points to enable visual comparisons of similar relative

619   positions along the cell boundary at the two time points. The blue line is the DTRH at the initial

620   time-point and dotted green line is DTRH at the final time-point. The time points in D to F,

621   correspond to those of A to C, respectively, and are shown in the legend for each of the plots.

622   The blue dots and red boxes on the x-axis identify lobe locations in the initial and final time

623   points, respectively. Scale bar, 20μm

624

625

626   Supplemental Data Figure Legends

627   Supplemental Figure S1. Examples of raw confocal images of pavement cells and

628   skeletonization results for the 15 cells that were used to validate LobeFinder.

629   **(A)** Raw images of epidermal cells. The cells segmented in yellow were used as the training set.

630   **(B)** Skeletonization results for the 15 test cells. Scale bar, 20μm.

631

632   Supplemental Figure S2. Sensitivity and accuracy analysis of LobeFinder performance.

633   **(A)** Definitions of sensitivity and False Discovery Rate (FDR).

634   **(B)** Sensitivity of LobeFinder outputs over a range of parameter values.

635   **(C)** FDR of LobeFinder outputs over a range of parameter values.

636

637   Supplemental Figure S3. Snapshot of the graphical user interface of LobeFinder. Operation steps

638   and navigation of the results are outlined.

639

640

641

642

Table 1   Lobe number quantification for cotyledon pavement cells at different developmental stages using LobeFinder

645

	38 to 55 HAG*		48 to 120 HAG		72 to 120 HAG	
	38 H	55 H	48 H	120 H	72 H	120 H
Averaged lobe number	9.60 ± 2.68	12.10 ± 2.99	8.27 ± 2.89	10.87 ± 2.59	11.17 ± 2.89	11.67 ± 2.46
Percent with lobe initiation	80		93		33	
Average new lobes per cell	2.50 ± 2.46		2.60 ± 1.68		0.50±2.07	

* For 38 to 55 HAG, N=10 cells, 48 to 120 HAG N=12 cells, 72 to 120 HAG N=12 cells

647

648

649

Table 2   Cell shape descriptors of cells analyzed with LobeFinder

651

	38 to 55 HAG		48 to 120 HAG		72 to 120 HAG	
	38 H	55 H	48 H	120 H	72 H	120 H
Circularity	0.60 ± 0.09	0.46 ± 0.11	0.62 ± 0.10	0.49 ± 0.11	0.45 ± 0.13	0.42 ± 0.12
Roundness	0.69 ± 0.06	0.63 ± 0.06	0.70 ± 0.09	0.64 ± 0.09	0.63 ± 0.08	0.61 ± 0.07
Convexity	0.93 ± 0.04	0.85 ± 0.07	0.94 ± 0.03	0.87 ± 0.06	0.84 ± 0.10	0.82 ± 0.10
Solidity	0.86 ± 0.03	0.79 ± 0.05	0.85 ± 0.06	0.80 ± 0.06	0.77 ± 0.06	0.75 ± 0.05

652

653

654

Parsed Citations

Ambrose JC, Shoji T, Kotzer AM, Pighin JA, Wasteneys GO (2007) The Arabidopsis CLASP gene encodes a microtubule-associated protein involved in cell expansion and division. Plant Cell 19: 2763-2775
Pubmed: Author and Title
CrossRef: Author and Title
Google Scholar: Author Only Title Only Author and Title

Andriankaja M, Dhondt S, De Bodt S, Vanhaeren H, Coppens F, De Milde L, Muhlenbock P, Skirycz A, Gonzalez N, Beemster GT, Inze D (2012) Exit from proliferation during leaf development in Arabidopsis thaliana: a not-so-gradual process. Dev. Cell 22: 64-78
Pubmed: Author and Title
CrossRef: Author and Title
Google Scholar: Author Only Title Only Author and Title

Arganda-Carreras I, Fernandez-Gonzalez R, Munoz-Barrutia A, Ortiz-De-Solorzano C (2010) 3D reconstruction of histological sections: Application to mammary gland tissue. Microsc Res Tech 73: 1019-1029
Pubmed: Author and Title
CrossRef: Author and Title
Google Scholar: Author Only Title Only Author and Title

Armour WJ, Barton DA, Law AM, Overall RL (2015) Differential growth in periclinal and anticlinal walls during lobe formation in Arabidopsis cotyledon pavement cells. Plant Cell 27: 2484-2500
Pubmed: Author and Title
CrossRef: Author and Title
Google Scholar: Author Only Title Only Author and Title

Asl LK, Dhondt S, Boudolf V, Beemster GTS, Beeckman T, Inze D, Govaerts W, De Veylder L (2011) Model-based analysis of Arabidopsis leaf epidermal cells reveals distinct division and expansion patterns for pavement and guard cells. Plant Physiol. 156: 2172-2183
Pubmed: Author and Title
CrossRef: Author and Title
Google Scholar: Author Only Title Only Author and Title

Backhaus A, Kuwabara A, Bauch M, Monk N, Sanguinetti G, Fleming A (2010) LEAFPROCESSOR: a new leaf phenotyping tool using contour bending energy and shape cluster analysis. New Phytol 187: 251-261
Pubmed: Author and Title
CrossRef: Author and Title
Google Scholar: Author Only Title Only Author and Title

Blilou I, Xu J, Wildwater M, Willemsen V, Paponov I, Friml J, Heidstra R, Aida M, Palme K, Scheres B (2005) The PIN auxin efflux facilitator network controls growth and patterning in Arabidopsis roots. Nature Cell Biol. 433: 39-44
Pubmed: Author and Title
CrossRef: Author and Title
Google Scholar: Author Only Title Only Author and Title

Delibaltov D, Gaur U, Kim J, Kourakis M, Newman-Smith E, Smith W, Belteton SA, Szymanski DB, Manjunath BS (2016) CellECT: Cell Evolution Capturing Tool. BMC Bioinformatics 17: 88
Pubmed: Author and Title
CrossRef: Author and Title
Google Scholar: Author Only Title Only Author and Title

Djakovic S, Dyachok J, Burke M, Frank MJ, Smith LG (2006) BRICK1/HSPC300 functions with SCAR and the ARP2/3 complex to regulate epidermal cell shape in Arabidopsis. Development 133: 1091-1100
Pubmed: Author and Title
CrossRef: Author and Title
Google Scholar: Author Only Title Only Author and Title

Elsner J, Michalski M, Kwiatkowska D (2012) Spatiotemporal variation of leaf epidermal cell growth: a quantitative analysis of Arabidopsis thaliana wild-type and triple cyclinD3 mutant plants. Ann Bot 109: 897-910
Pubmed: Author and Title
CrossRef: Author and Title
Google Scholar: Author Only Title Only Author and Title

Fu Y, Gu Y, Zheng Z, Wasteneys GO, Yang Z (2005) Arabidopsis interdigitating cell growth requires two antagonistic pathways with opposing action on cell morphogenesis. Cell 11: 687-700
Pubmed: Author and Title
CrossRef: Author and Title
Google Scholar: Author Only Title Only Author and Title

Fu Y, Li H, Yang Z (2002) The ROP2 GTPase controls the formation of cortical fine F-actin and the early phase of directional cell expansion during Arabidopsis organogenesis. Plant Cell 14: 777-794
Pubmed: Author and Title
CrossRef: Author and Title
Google Scholar: Author Only Title Only Author and Title

Gao Y, Zhang Y, Zhang D, Dai X, Estelle M, Zhao Y (2015) Auxin binding protein 1 (ABP1) is not required for either auxin signaling or Arabidopsis development. Proc. Natl. Acad. Sci. U S A 112: 2275-2280
Pubmed: Author and Title
CrossRef: Author and Title

Google Scholar: Author Only Title Only Author and Title

Geitmann A, Ortega JK (2009) Mechanics and modeling of plant cell growth. Trends Plant Sci. 14: 467-478
Pubmed: Author and Title
CrossRef: Author and Title
Google Scholar: Author Only Title Only Author and Title

Graham RL (1972) An efficient algorith for determining the convex hull of a finite planar set. Information processing letters 1: 132-133
Pubmed: Author and Title
CrossRef: Author and Title
Google Scholar: Author Only Title Only Author and Title

Jura J, Kojs P, Iqbal M, Szymanowska-Pulka J, Wloch W (2006) Apical intrusive growth of cambial fusiform initials along the tangential walls of adjacent fusiform initials: evidence for a new concept. Aust. J. Bot. 54: 493-504
Pubmed: Author and Title
CrossRef: Author and Title
Google Scholar: Author Only Title Only Author and Title

Kieber J, Rothenberg M, Roman G, Feldmann K, Ecker J (1993) CTR1, a negative regulator of the ethylene response pathway in Arabidopsis, encodes a member of the Raf family of protein kinases. Cell 72: 427-441
Pubmed: Author and Title
CrossRef: Author and Title
Google Scholar: Author Only Title Only Author and Title

Kirik V, Herrmann U, Parupalli C, Sedbrook JC, Ehrhardt DW, Hulskamp M (2007) CLASP localizes in two discrete patterns on cortical microtubules and is required for cell morphogenesis and cell division in Arabidopsis. J Cell Sci 120: 4416-4425
Pubmed: Author and Title
CrossRef: Author and Title
Google Scholar: Author Only Title Only Author and Title

Kuchen EE, Fox S, de Reuille PB, Kennaway R, Bensmihen S, Avondo J, Calder GM, Southam P, Robinson S, Bangham A, Coen E (2012) Generation of leaf shape through early patterns of growth and tissue polarity. Science 335: 1092-1096
Pubmed: Author and Title
CrossRef: Author and Title
Google Scholar: Author Only Title Only Author and Title

Le J, El-Assal SE, Basu D, Saad ME, Szymanski DB (2003) Requirements for Arabidopsis ATARP2 and ATARP3 during epidermal development. Curr. Biol. 13: 1341-1347
Pubmed: Author and Title
CrossRef: Author and Title
Google Scholar: Author Only Title Only Author and Title

Le J, Mallery EL, Zhang C, Brankle S, Szymanski DB (2006) Arabidopsis BRICK1/HSPC300 is an essential WAVE-complex subunit that selectively stabilizes the Arp2/3 activator SCAR2. Curr. Biol. 16: 895-901
Pubmed: Author and Title
CrossRef: Author and Title
Google Scholar: Author Only Title Only Author and Title

Lin D, Cao L, Zhou Z, Zhu L, Ehrhardt D, Yang Z, Fu Y (2013) Rho GTPase signaling activates microtubule severing to promote microtubule ordering in Arabidopsis. Curr. Biol. 23: 290-297
Pubmed: Author and Title
CrossRef: Author and Title
Google Scholar: Author Only Title Only Author and Title

Ma W-Y, Manjunath BS (2000) EdgeFlow: a technique for boundary detection and image segmentation. Image Processing, IEEE Transactions on 9: 1375-1388
Pubmed: Author and Title
CrossRef: Author and Title
Google Scholar: Author Only Title Only Author and Title

Marcuzzo M, Quelhas P, Campilho A, Mendonça AM (2008) Automatic cell segmentation from confocal microscopy images of the Arabidopsis root. In Biomedical Imaging: From Nano to Macro, 2008. ISBI 2008. 5th IEEE International Symposium on. IEEE, pp 712-715
Pubmed: Author and Title
CrossRef: Author and Title
Google Scholar: Author Only Title Only Author and Title

Panteris E, Apostolakos P, Galatis B (1993) Microtubules and morphogenesis in ordinary epidermal cells of Vigna sinensis leaves. Protoplasma 174: 91-100
Pubmed: Author and Title
CrossRef: Author and Title
Google Scholar: Author Only Title Only Author and Title

Panteris E, Galatis B (2005) The morphogenesis of lobed plant cells in the mesophyll and epidermis: organization and distinct roles of cortical microtubules and actin filaments. New Phytol. 167: 721-732
Pubmed: Author and Title
CrossRef: Author and Title
Google Scholar: Author Only Title Only Author and Title

Qiu JL, Jilk R, Marks MD, Szymanski DB (2002) The Arabidopsis SPIKE1 gene is required for normal cell shape control and tissue

development. Plant Cell 14: 101-118

Pubmed: Author and Title
CrossRef: Author and Title
Google Scholar: Author Only Title Only Author and Title

Remmler L, Rolland-Lagan AG (2012) Computational method for quantifying growth patterns at the adaxial leaf surface in three dimensions. Plant Physiol 159: 27-39

Pubmed: Author and Title
CrossRef: Author and Title
Google Scholar: Author Only Title Only Author and Title

Robert C, Noriega A, Tocino Á, Cervantes E (2008) Morphological analysis of seed shape in Arabidopsis thaliana reveals altered polarity in mutants of the ethylene signaling pathway. Journal of plant physiology 165: 911-919

Pubmed: Author and Title
CrossRef: Author and Title
Google Scholar: Author Only Title Only Author and Title

Roeder AH, Chickarmane V, Cunha A, Obara B, Manjunath BS, Meyerowitz EM (2010) Variability in the control of cell division underlies sepal epidermal patterning in Arabidopsis thaliana. PLoS Biol 8: e1000367

Pubmed: Author and Title
CrossRef: Author and Title
Google Scholar: Author Only Title Only Author and Title

Russ JC (2002) The Image Processing Handbook, Ed Fourth. CRC Press, Boca Raton

Pubmed: Author and Title
CrossRef: Author and Title
Google Scholar: Author Only Title Only Author and Title

Sampathkumar A, Krupinski P, Wightman R, Milani P, Berquand A, Boudaoud A, Hamant O, Jonsson H, Meyerowitz EM (2014) Subcellular and supracellular mechanical stress prescribes cytoskeleton behavior in Arabidopsis cotyledon pavement cells. Elife (Cambridge) 3: e01967

Pubmed: Author and Title
CrossRef: Author and Title
Google Scholar: Author Only Title Only Author and Title

Savaldi-Goldstein S, Peto C, Chory J (2007) The epidermis both drives and restricts plant shoot growth. Nature 446: 199-202

Pubmed: Author and Title
CrossRef: Author and Title
Google Scholar: Author Only Title Only Author and Title

Schindelin J, Arganda-Carreras I, Frise E, Kaynig V, Longair M, Pietzsch T, Preibisch S, Rueden C, Saalfeld S, Schmid B (2012) Fiji: an open-source platform for biological-image analysis. Nature methods 9: 676-682

Pubmed: Author and Title
CrossRef: Author and Title
Google Scholar: Author Only Title Only Author and Title

Staff L, Hurd P, Reale L, Seoighe C, Rockwood A, Gehring C (2012) The hidden geometries of the Arabidopsis thaliana epidermis. PLoS One 7: e43546

Pubmed: Author and Title
CrossRef: Author and Title
Google Scholar: Author Only Title Only Author and Title

Szymanski DB, Cosgrove DJ (2009) Dynamic coordination of cytoskeletal and cell wall systems during plant cell morphogenesis. Curr. Biol. 19: R800-R811

Pubmed: Author and Title
CrossRef: Author and Title
Google Scholar: Author Only Title Only Author and Title

Szymanski DB (2014) The kinematics and mechanics of leaf expansion: new pieces to the Arabidopsis puzzle. Curr. Opin. Plant Biol. 22C: 141-148

Pubmed: Author and Title
CrossRef: Author and Title
Google Scholar: Author Only Title Only Author and Title

Tsuge T, Tsukaya H, Uchimiya H (1996) Two independent and polarized processes of cell elongation regulate leaf blade expansion in Arabidopsis thaliana (L.) Heynh. Development 122: 1589-1600

Pubmed: Author and Title
CrossRef: Author and Title
Google Scholar: Author Only Title Only Author and Title

Walter A, Silk WK, Schurr U (2009) Environmental effects on spatial and temporal patterns of leaf and root growth. Annu Rev Plant Biol 60: 279-304

Pubmed: Author and Title
CrossRef: Author and Title
Google Scholar: Author Only Title Only Author and Title

Xu T, Wen M, Nagawa S, Fu Y, Chen JG, Wu MJ, Perrot-Rechenmann C, Friml J, Jones AM, Yang Z (2010) Cell surface- and rho GTPase-based auxin signaling controls cellular interdigitation in Arabidopsis. Cell 143: 99-110

Pubmed: Author and Title
CrossRef: Author and Title
Google Scholar: Author Only Title Only Author and Title

Yoder N (2011) PeakFinder. Internet: http://www.mathworks.com-/matlabcentral/fileexchange/25500
Pubmed: Author and Title
CrossRef: Author and Title
Google Scholar: Author Only Title Only Author and Title

Zhang C, Halsey L, Szymanski DB (2011) The development and geometry of shape change in Arabidopsis thaliana cotyledon pavement cells. BMC Plant Biol. 11: 27
Pubmed: Author and Title
CrossRef: Author and Title
Google Scholar: Author Only Title Only Author and Title

Zhang C, Mallery EL, Schlueter J, Huang S, Fan Y, Brankle S, Staiger CJ, Szymanski DB (2008) Arabidopsis SCARs function interchangeably to meet actin-related protein 2/3 activation thresholds during morphogenesis. Plant Cell 20: 995-1011
Pubmed: Author and Title
CrossRef: Author and Title
Google Scholar: Author Only Title Only Author and Title

Zhu XG, Long SP, Ort DR (2010) Improving photosynthetic efficiency for greater yield. Annu Rev Plant Biol 61: 235-261
Pubmed: Author and Title
CrossRef: Author and Title
Google Scholar: Author Only Title Only Author and Title